# Measurement of Moisture Distribution in a Biomass Silo through Electrical Capacitance Tomography

Ge Guo, Yong Yan, *Fellow, IEEE*, Wenbiao Zhang, *Senior Member, IEEE,*
Yonghui Hu, *Senior Member, IEEE,* and Guimei Fu

*Abstract*—**The moisture distribution in stored biomass is a key factor in the self-heating and spontaneous combustion of biomass fuels. Measurement of moisture distribution in biomass fuels is thus essential for the safe operation of biomass-fired power plants. As a non-invasive imaging technique, electrical capacitance tomography (ECT) is proposed to measure the moisture distribution in stored wood pellets. The moisture distribution in different shapes and locations is measured on a laboratory-scale silo. Tomographic reconstruction algorithms are applied to obtain a visual representation of the moisture distribution. The relationship between the moisture content and effective permittivity of wood pellets is experimentally established. Experimental results demonstrate that ECT is capable of measuring the wet area ranging from 4% to 93% with a relative error of ±8%. The centroid position of the moisture distribution is measured with a relative error of ±5%. Meanwhile, the measured moisture content of the wet area has a relative error of ±10% over the range of 7.7%~16.4%.**

*Index Terms*—**Biomass, moisture distribution, electrical capacitance tomography, image reconstruction.**

## I. INTRODUCTION

**B**IOMASS accounts for approximately 9.4% of the global energy supply [1]. Wood pellets are widely used in biomass-fired power plants owing to their advantages of renewability, high calorific value and low emissions [2]. The self-heating and spontaneous combustion of wood pellets are important issues related to the safe operation of biomass-fired power plants [3]. If wood pellets have an inconsistent distribution of moisture content, some wet regions will lead to localized hotspots due to microbial activity, chemical reactions, or other factors [4]. The heat generated can accumulate, eventually reaching the ignition temperature of biomass. Once ignition occurs, a fire will spread rapidly, causing significant damage and posing a safety risk [3]. Therefore, it is important to develop a reliable and effective method for the online continuous measurement of moisture distribution in wood pellets.

A number of methods based on different sensing principles have been developed in the past to measure the moisture distribution in bulk materials. Mao *et al.* [5] investigated a low-field nuclear magnetic resonance method for measuring the moisture distribution in sludge. However, the high cost, potential radiation hazard and sophistication of the system make this method unsuitable for the intended application [6]. Klingmuller *et al.* [7] used a deep neural network to predict the moisture distribution of soil, applying meteorological data from a climate model. However, this method requires a large volume of sample data, which restricts the wider application of this method. Near-infrared imaging (NIR) was used for deriving the moisture distribution in pharmaceutical wet granules [8]. However, NIR measures the surface or shallow-layer information of the material. In addition, the effects of material size, surface characteristics and surface color result in measurement errors. These factors make NIR unsuitable for real-time measurement of moisture distribution in an industrial silo.

In recent years, electrical resistance tomography (ERT) [9], electromagnetic tomography (EMT) [10] and electrical capacitance tomography (ECT) [11] have been applied to measuring the moisture distribution in bulk solids. However, ERT requires good ohmic contact between the object surface and the measured electrode, which is applied to bulk solids with high moisture content [12]. EMT is suitable for imaging objects that have high permeability, while it has difficulty obtaining the moisture content [13]. In contrast, ECT does not need ohmic contact with the target surface and is suitable for bulk solids with low moisture content. ECT is mainly used to measure the moisture distribution in fluidized beds [14], pipe sections [15] and other industrial settings [16]. ECT was utilized for measuring the moisture distribution of pharmaceutical granules in a conical product bowl [17]. Wang et al. [18] used ECT to measure the solids distribution and moisture content in a fluidized bed dryer. To date there is little research on the application of ECT to a bulk solids material in a large silo. Wood pellets are widely used for power generation. Such bulk solids contain many small channels with non-uniform dielectric properties [19]. In this paper, ECT is proposed for the first time to measure the moisture content and its distribution of wood pellets in an octagon silo. There is currently no practically

workable solution to the measurement problem. ECT is a non-invasive, cost-effective measurement method that may provide the moisture distribution measurement in a non-circular biomass silo, including size of the moist area and its location in the silo, in addition to the moisture content. Measuring the wet area in the silo is important to inform the plant operators about the size of the moist area and its potential self-heating risks they are taking. The centroid position of the moist area is to notify the users where the wet region is located in the silo so that appropriate action can be taken to reduce self-heating and hence fire risks. The moisture content of the moist region allows the users to assess the degree of moisture level and take cost-effective actions about the wet area. All three variables are important to power plant operators. To the best of our knowledge, there are few techniques available that can measure these quantities to reduce fire risks at biomass power plants.

Moisture content affects the dielectric properties of biomass material, resulting in variations in permittivity. Some researchers used capacitive sensors to measure the moisture content of materials. For instance, Zhang *et al*. [20] used a helical capacitive sensor to measure the moisture content of woodchips. Dean *et al.* [21] utilized a capacitive fringing field sensor to measure the moisture content in soil. Santos *et al.* [22] presented a high-precision capacitive sensor to measure the moisture content of polymers. However, there is little literature on measuring the permittivity and moisture content in wood pellets. In this paper, ECT is applied for the first time to obtain moisture content and moisture distribution of the wood pellets in a silo. The functional relationship between the moisture content and permittivity of wood pellets is established through a series of experiments. Based on the reconstructed results from the ECT system, the moisture distribution in a biomass silo is determined.

The preliminary experimental results of moisture distribution measurement and optimization of capacitive sensors were first reported at the IEEE International Instrumentation Measurement Technology Conference in 2023 [23]. This article presents in detail the fundamental principle, sensor design, implementation and experimental assessment of the proposed measurement system.

## II. MEASUREMENT PRINCIPLE AND CAPACITIVE SENSOR DESIGN

### A. *Overall strategy*

The permittivity of wood is between 2 and 6, and the permittivity of water is approximately 80 [24]. Due to the large difference in permittivity between wood and water, moisture content is a key factor affecting the permittivity of wood pellets [25]. Therefore, ECT is applied to measure the moisture content and moisture distribution in a biomass silo. Based on the measured capacitance values between a set of electrodes, the measurement system is capable of reconstructing the permittivity distribution in the sensing field.

### B. *Sensor design*

When an ECT system is used to measure the moisture distribution in a bulk solids storage unit, the cross-sectional
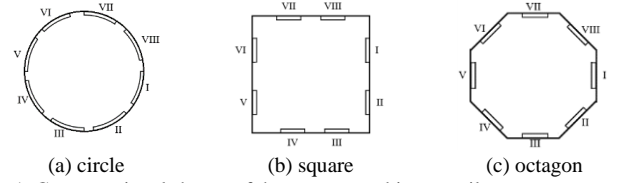


(a) circle      (b) square      (c) octagon
Fig. 1. Cross-sectional shapes of three common biomass silos.
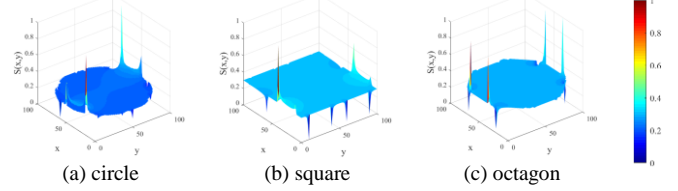


(a) circle      (b) square      (c) octagon
Fig. 2 Sensitivity distribution between the electrodes I and V for the three cross-sectional silo shapes.
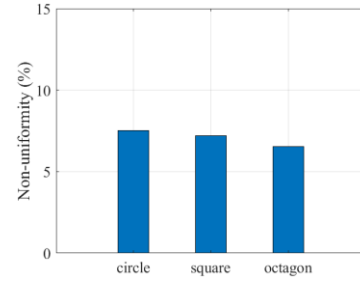


Fig. 3. Comparison of non-uniformity for different silo shapes.
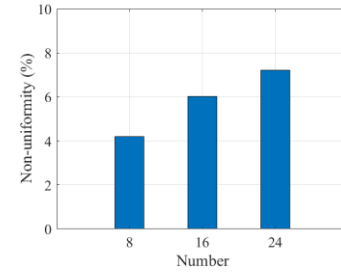


Fig.4. Comparison of non-uniformity for different numbers of electrodes.
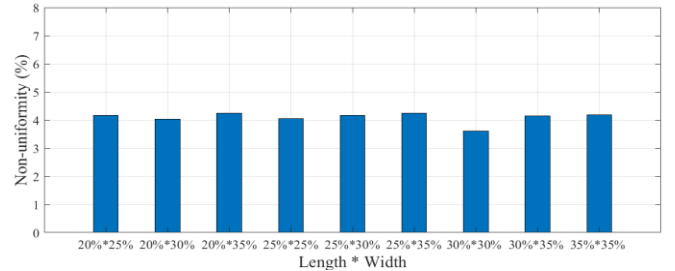


Fig. 5. Comparison of non-uniformity for different sized electrodes.

shape of the unit and the optimization of the capacitive sensors have significant effects on the performance of the measurement system. A term, called non-uniformity, is introduced to evaluate the uniformity of the sensitivity distribution in the capacitive sensing field [26], which is defined as:

$$\text{non-uniformity} = \frac{\widetilde{S(x,y)}}{\overline{S(x,y)}} \times 100\% \qquad (1)$$

where $\widetilde{S(x,y)}$ is the standard deviation of the sensitivity and $\overline{S(x,y)}$ indicates the average sensitivity across the sensing field.

Biomass silos in power plants are usually in the form of cylindrical, cuboidal and octagonal shapes [27]. Comparing different shapes of biomass silos in terms of sensitivity distribution for the same number of electrodes is useful to

quantify their differences in their sensing field homogeneity. It should be noted that we are not trying to optimize the design of a silo here as this is given in practice. However, it is useful to know their differences in the sensitivity distribution of an ECT system with the same number of electrodes. Since most biomass silos are made of metal materials, the electrodes should be mounted on the inner walls of the silo. Therefore, the three different silo shapes are all considered in this study, as shown in Fig. 1. As expected, different shaped silos have different sensitivity distributions due to the physical distribution of the electrodes on the silo walls. For instance, when electrodes I and V are the excitation and measuring electrodes, respectively, the resulting sensitivity distribution of the three cross-sectional shapes is shown in Fig. 2.

The electrodes are mounted on the inner walls of the biomass silo. Based on the finite element analysis of the sensing system, the sensitivity distributions of all electrodes across each silo are determined. By calculating the standard deviation and average value of the sensitivity distribution, the non-uniformity of the sensing field is obtained. Fig. 3 shows a comparison of the non-uniformity for the three different silo shapes. From (1), as the standard deviation decreases or average sensitivity increases, the non-uniformity decreases, indicating a more uniform sensitivity distribution (Fig. 2). In other words, the octagonal silo has the best sensing field uniformity amongst the three. In practice, there are more cylindrical biomass silos than octagon ones. However, an octagon silo is used in this study as it is easy to construct for the experimental research under laboratory conditions.

For an octagonal silo, each flat side of the silo can fit one, two, three or more electrodes, making the total number of electrodes 8, 16, 24 or more. Fig. 4 depicts a comparison of the non-uniformity for different numbers of electrodes in the octagonal silo. It is evident that the non-uniformity of the eight-electrode design is smaller than the other two. Meanwhile, eight electrodes are chosen instead of other options in consideration of the computational load and efficiency of image reconstruction algorithms.

For an ECT system, it is important to optimize the size of the electrodes. In view of the practical applications and convenience of the sensor design, the length and width of the electrodes are expressed as a percentage of the silo side length. Based on an orthogonal experimental design [28], nine different electrode sizes are considered. The non-uniformity of different sized electrodes is shown in Fig. 5. It is clear that electrodes with a length and width of 30% of the silo side length exhibit the smallest non-uniformity amongst the nine sizes. These dimensions of the electrodes are, therefore, used to build an experimental setup in this study.

## III. PERMITTIVITY AND MOISTURE CONTENT

### A. Experimental setup

According to the sensor optimization results, an experimental setup was designed and built, as shown in Fig. 6. The experimental octagonal silo is made of eight aluminum plates with a height of 100 cm and a width of 100 cm. The electrodes


(a) Octagonal silo.  (b) Electrodes.
(c) Measurement system.
Fig. 6 Experimental setup.
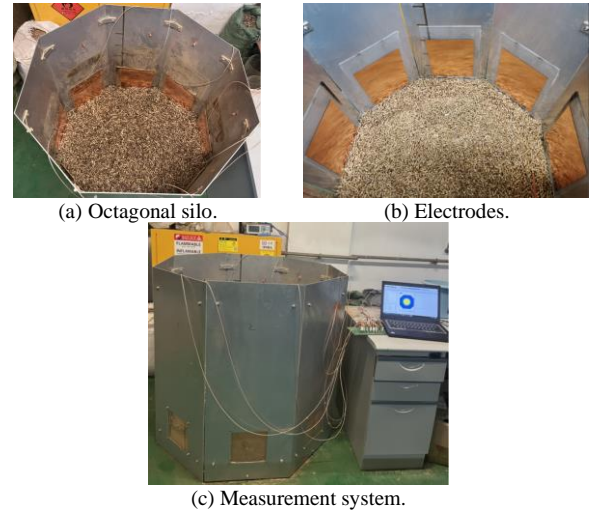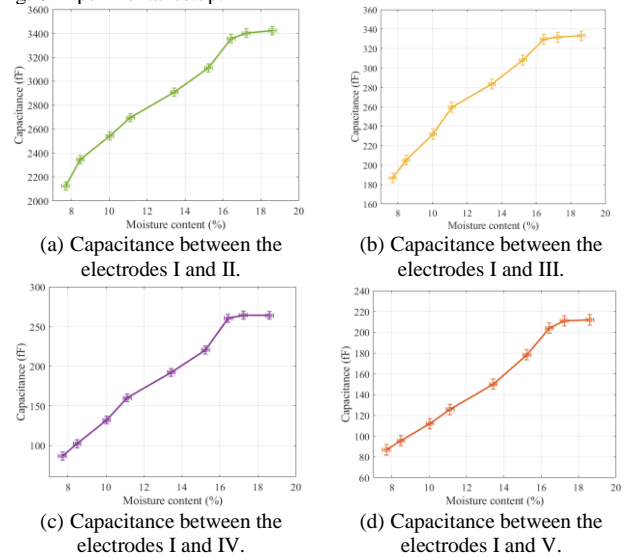

(a) Capacitance between the electrodes I and II.  (b) Capacitance between the electrodes I and III.
(c) Capacitance between the electrodes I and IV.  (d) Capacitance between the electrodes I and V.
Fig. 7. Variations in capacitance with moisture content between different electrode pairs.
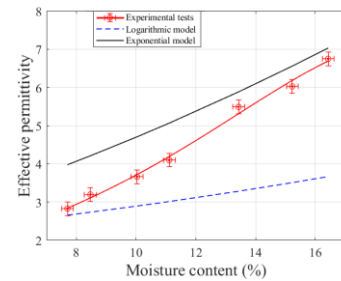

Fig. 8. Variations in effective permittivity with moisture content.

for the ECT are made from copper foil and mounted on the inner walls of the silo. A capacitance-to-digital chip PCap01 is used to measure the capacitance values between all the electrodes.

### B. Effective permittivity

Pelletized biomass generates less particulate emissions when compared to its original form or other traditional biomass fuels [29]. The flexible size and higher calorific value make it easier to be transported and stored, compared to raw materials [30]. Wood pellets are commonly used for power generation across the world. For this reason, wood pellets were used as experimental materials.

Permittivity measurement plays a crucial role in obtaining the moisture content of wood pellets [31]. The effective permittivity of a mixture is determined by the permittivity of the individual components and their volume fractions. In order to obtain the effective permittivity of wood pellets with different moisture content, the exponential model [32] and the logarithmic model [33] are used to calculate the theoretical effective permittivity. For a mixture, these two models are widely used, and the calculated permittivity is closer to the actual value [34]. The exponential model is presented as follows:

$$\varepsilon^{\beta} = \sum_l (\theta_l \cdot \varepsilon_l^{\beta}) \tag{2}$$

where $\varepsilon$ stands for the permittivity of the mixture, $\beta$ is a constant, $l$ represents the type of component material, $\varepsilon_l$ indicates the permittivity of material $l$, and $\theta_l$ means the volume fraction of material $l$.

The logarithmic model is expressed as:

$$\varepsilon = \prod_l (\varepsilon^{\theta_l}) \tag{3}$$

### C. Calibration experiments

In preparation of the wood pellets to be tested with different moisture contents, the mass of required water was obtained, based on the weight moisture content [35]. Then, the water was evenly sprayed onto dry wood pellets. Ventilation minimizes moisture variations and ensures that the moisture in the wood pellets is in equilibrium with the surrounding environment. After the ventilation process, 10 small samples were selected. A commercial moisture analyzer (Mettler Toledo, HE83) was used to obtain the reference moisture content of these samples. Finally, the silo was filled slowly with the wood pellets until the height of wood pellets reached 60 cm. By repeating the above process, the wood pellets with different moisture contents in the silo were realized.

It is worth noting that packing volume fraction of wood pellets in the silo can also affect the mixture permittivity in addition to moisture content. The wood pellets tested are of cylindrical shape with a diameter of approximately 1 cm and a length ranging from 2 cm to 5 cm. In earlier work on acoustic temperature measurement [36], it was found that, when the height of wood pellets in a container exceeds 50 cm, the average pore between wood pellets is little affected by the height of wood pellets. In this paper, the height of the wood pellets in the silo is 60 cm, so the packing density of wood pellets in the silo can be assumed constant. The wood pellets were handled carefully during the filling process to ensure the packing volume fraction of wood pellets remains more or less the same.

Under normal laboratory conditions, the moisture content of wood pellets was measured to be 7.7%, which is used as a baseline for the moisture content of dry wood pellets. The moisture content of wood pellets in the power industry ranges typically from 11% to 13% [37]. The whole wood pellet sample was split into eight smaller portions. After ten repeated measurements, the mean moisture content of each portion was measured to be 8.5%, 9.9%, 11.1%, 13.3%, 15.3%, 16.4%, 17.2% and 18.6%, respectively. The variations in the capacitance value with moisture content for four types of physical arrangement between the electrodes, e.g., electrode pairs I-II, I-III, I-IV, and I-V (Fig. 1(c)) are shown in Fig. 7.

Fig. 7 depicts the variations in the capacitance of the wood pellets with moisture content. The standard deviation of the ten

Table I Comparison of reconstructed images for different algorithms.



| Wet area (%) | Targeted distribution | LBP | Tikhonov | Landweber | SIRT | FSBI | Moisture content |
|---|---|---|---|---|---|---|---|
| 4 | | | | | | | |
| 9 | | | | | | | |
| 25 | | | | | | | |
| 81 | | | | | | | |



(a) Wet area.   (b) Moisture content.

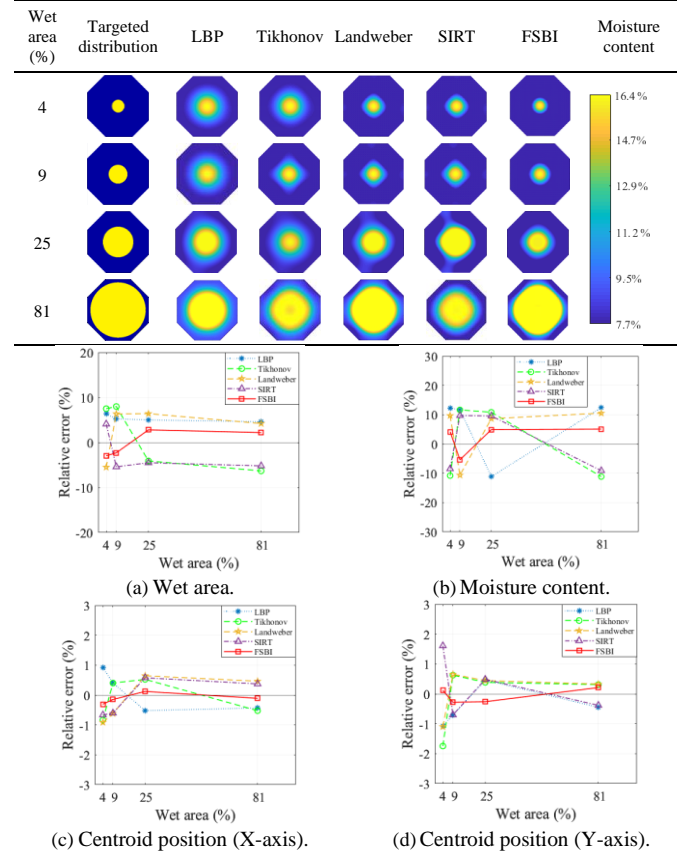(c) Centroid position (X-axis).   (d) Centroid position (Y-axis).

Fig. 9. Relative errors of the wet area, moisture content and centroid position for the five reconstruction algorithms.

Table II Comparison of execution runtime for different algorithms (unit: s).

| Wet area | LBP | Tikhonov | Landweber | SIRT | FSBI |
|---|---|---|---|---|---|
| 4% | 0.08 | 5.23 | 6.62 | 6.74 | 5.93 |
| 9% | 0.08 | 5.18 | 6.53 | 6.73 | 6.07 |
| 50% | 0.08 | 5.20 | 6.54 | 6.69 | 5.92 |
| 81% | 0.08 | 5.19 | 6.55 | 6.68 | 5.84 |

moisture measurements is represented as an 'error' bar in Fig. 7. It can be seen from Fig. 7 that, when the moisture content of wood pellets is greater than 16.4%, the capacitance value tends to be constant. Wood pellets are produced by compressing dry wood fibers [38]. When the moisture content of wood pellets is higher than 16.4%, the wood pellets in the silo will become soaking wet wood fibers and dust. Since the focus of this research is to measure the moisture content and its distribution of moist wood pellets in a silo, the range of moisture content in this study is between 7.7% and 16.4%.

The effective permittivity of a mixture depends on the permittivity of the individual components and their volume fractions in the mixture. The volume fractions of wood pellets and air are constant in the silo. The permittivity of water is much larger than that of wood and air. Although there are three different materials in the silo, we are interested in the effect of water on the permittivity. A series of experiments was carried out to establish the functional relationship between the moisture content and effective permittivity. The moisture contents of wood pellet portions were 8.5%, 9.9%, 11.1%, 13.3%, 15.3% and 16.4%, respectively. Based on the reconstructed results from the ECT system, the effective permittivity of wood pellets with different moisture contents were obtained, as shown in Fig.

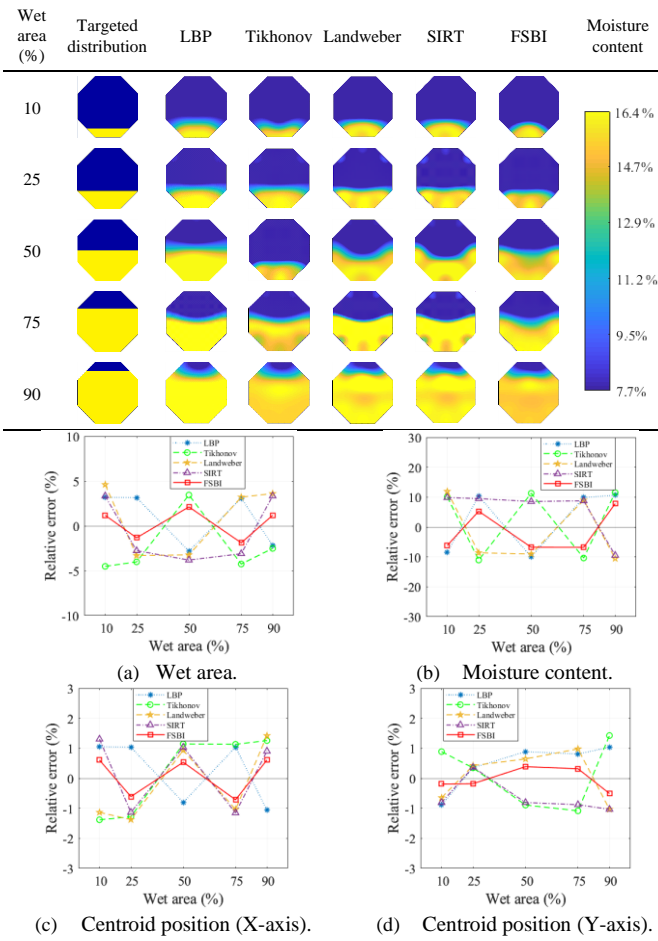Table III Reconstructed results of the segmented moisture distributions.



Fig. 10. Relative errors of the wet area, moisture content and centroid position for the segmented moisture distributions.

Table IV Reconstructed images of the oblique moisture distributions.



Fig. 11. Relative errors of the wet area, moisture content and centroid position for the oblique moisture distributions.

8. From (2) and (3), the effective permittivity of the exponential and logarithmic models is calculated and plotted in Fig. 8.

Fig. 8 exhibits the variations in the effective permittivity of wood pellets with moisture content. Each experimental data point in Fig. 8 is the mean of ten repeated measurements. The trends of the data are fitted with the rational polynomials [39] and plotted in Fig. 8. It can be seen that the effective permittivity increases with moisture content. These results are consistent with the conclusions from the theoretical values in [32-34]. As a result of the experimental tests, the effective permittivity of wood pellets is obtained with moisture content from 7.7% to 16.4%.

## IV. EXPERIMENT RESULTS AND DISCUSSION

### A. Image reconstruction

Image reconstruction algorithms are used to reconstruct the permittivity distribution in a biomass silo from the measured capacitance values. There are five commonly used algorithms for image reconstruction, i.e., the linear back projection (LBP) algorithm, the Tikhonov algorithm, the Landweber algorithm, the simultaneous iterative reconstruction technique (SIRT) and the fast iterative shrinkage thresholding (FSBI) [40].

Three parameters are introduced to assess the reconstructed moisture distribution in a biomass silo, which are wet area, centroid position and moisture content. The reconstructed

image is binarized with the Otsu threshold algorithm (OTSU) algorithm [41]. The relative error of the wet area between the reconstructed distribution and the actual distribution is calculated based on the number of pixels. The relative error between the actual and reconstructed centroid position is obtained from the binarized images. The relative error of the moisture content is calculated by comparing the reconstructed moisture content with the actual moisture content.

### B. Numerical simulation and results

In order to further validate the performance of the ECT, numerical simulations are conducted in the octagonal silo. The cross-sectional moisture distributions in a biomass silo are usually circular, segmented and oblique segmented distributions.

1) Case 1

Four circular areas of different sizes with high moisture content in the octagonal silo are used to implement numerical validations. The circular areas are 4%, 9%, 25% and 81% of the octagonal silo cross-section, respectively. The four targeted distributions are shown in Table I, in which the yellow color represents the high permittivity material ($\varepsilon = 6.8$) and the blue color represents the low permittivity material ($\varepsilon = 2.8$).

The regularization parameter of the Tikhonov algorithm is 0.3. The relaxation factor of the Landweber algorithm is 0.003

and the iterations are 2000. The weighting factor of the SIRT algorithm is 0.5 and the iterations are 1500. The penalty parameters of the FSBI algorithm are 0.2 and 0.01, and the iterations are 100. Table I depicts the reconstruction results from the LBP algorithm, the Tikhonov algorithm, the Landweber algorithm, the SIRT algorithm and the FSBI algorithm, respectively. Fig. 9 shows the relative errors of the wet area, centroid position and moisture content for the five reconstruction algorithms. Table II provides the execution runtime of the five image algorithms.

Through comparisons of the results in Table I, the reconstructed images using the LBP algorithm, the Tikhonov algorithm, the Landweber algorithm and the SIRT algorithm have many artifacts. The imaging results from the FSBI algorithm are the closest to the targeted distributions amongst the five algorithms. As non-iterative algorithms, the LBP algorithm and the Tikhonov algorithm have the advantages of simple implementation and low time costs. However, there are many artifacts in the reconstructed images. After multiple iterations, iterative algorithms have fewer artifacts, but the time consumption increases. As illustrated in Table II, the execution runtime of the FSBI algorithm is the shortest among the iterative algorithms. In conclusion, the FSBI algorithm provides good reconstructed images in a short time.

As illustrated in Fig. 9, the relative errors of the wet area, centroid position and moisture content from the FSBI algorithm are the smallest among the five algorithms. For the circular moisture distributions, the relative error of the wet area from the FSBI algorithm is within $\pm3\%$ and the relative error of the centroid position is within $\pm1\%$. Moreover, the relative error of the moisture content is within $\pm6\%$. These simulation results reconstructed with the FSBI algorithm are the best amongst the five algorithms. This is primarily due to the fact that L1 regularization improves the robustness of the FSBI algorithm, while Lp regularization enhances the sparsity of the targeted distributions [40].

2) *Case 2*

Five segmented distributions with high moisture content in the octagonal silo are utilized. The wet areas are 10%, 25%, 50%, 75% and 90% of the octagonal silo cross-section, respectively. The reconstructed images are shown in Table III. The relative errors of the wet area, centroid position and moisture content are illustrated in Fig. 10, respectively.

Table III reveals that the reconstructed images from the FSBI algorithm are more similar to the targeted distributions. Through a comparison of the results in Fig. 10, the relative errors of the wet area, centroid position and moisture content from the FSBI algorithm are smaller than those from the other four algorithms. Fig. 10(a) shows that the relative error of the wet area is within $\pm3\%$. Fig. 10(b) indicates that the relative error of the moisture content is within $\pm8\%$. In Fig. 10(c)-(d), the relative error of the centroid position is within $\pm1\%$.

3) *Case 3*

The moisture distribution in a biomass silo is a segmented distribution along a diagonal direction. Five oblique moisture distributions are used in the octagonal silo. The wet areas are 7%, 28%, 50%, 72% and 93% of the octagonal silo cross-section, respectively. Table IV depicts the reconstruction results.

Table V Comparison of reconstructed images for the circular moisture distributions.





(a) Wet area.  (b) Moisture content.

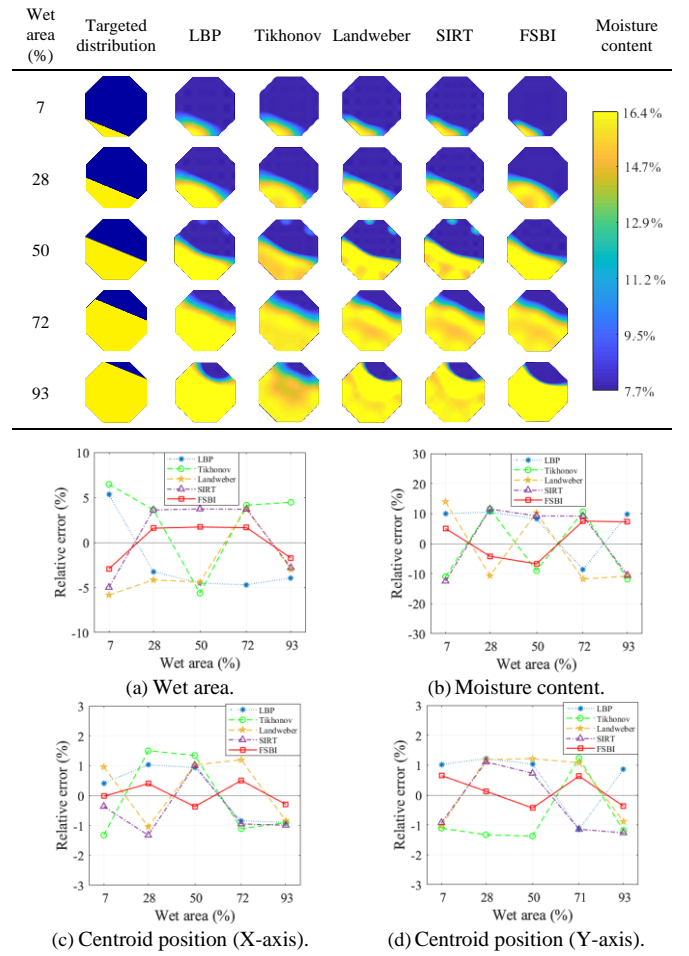(c) Centroid position (X-axis).  (d) Centroid position (Y-axis).
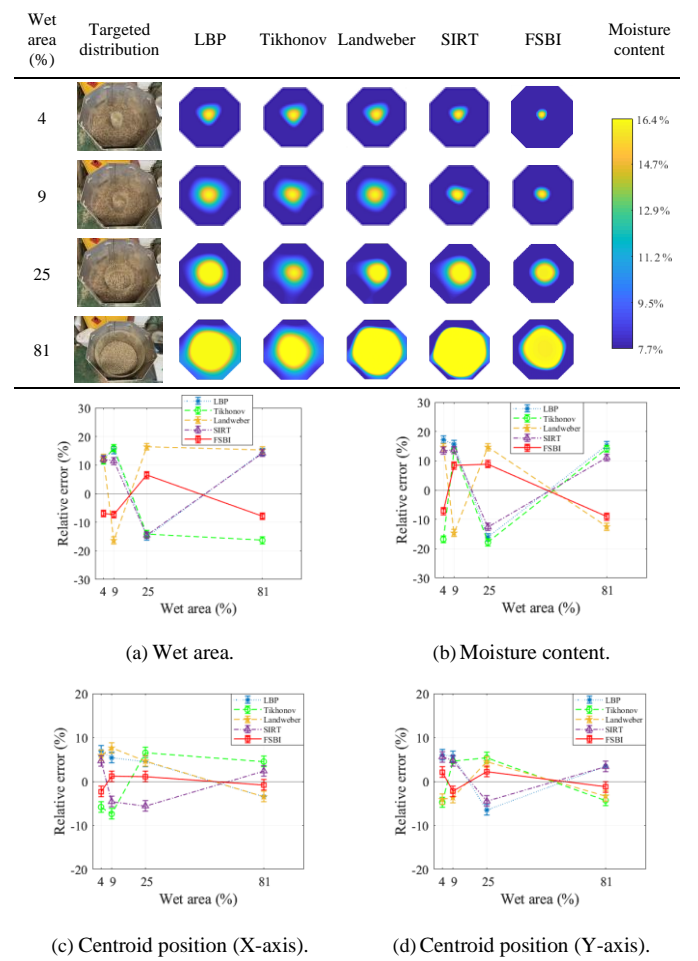
Fig. 12. Relative errors of the wet area, moisture content and centroid position for the circular moisture distributions.

Fig. 11 exhibits the relative errors of the wet area, centroid position and moisture content.

The reconstructed images in Table IV illustrate that the boundary between the dry wood pellets and the wet wood pellets in the reconstructed images using the FSBI algorithm is more obvious than those from other algorithms. It can be seen from Fig. 11 that the relative errors from the FSBI algorithm are the smallest. The reconstruction results reveal that the relative error of the wet area from the FSBI algorithm is within $\pm3\%$ and the relative error of the centroid position is within $\pm1\%$. Meanwhile, the relative error of the moisture content is within $\pm8\%$.

*C. Experimental Results*

In order to assess the performance of the ECT in measuring the moisture distribution in a biomass silo, a series of experiments was conducted. The variations in the moisture distribution along the height direction are ignored. During the experiments, the ambient temperature was 21℃, which was constant during the experiments. Based on the results shown in Fig. 8, the dry wood pellets (moisture content = 7.7%) are set as low permittivity, which is 2.8. Meanwhile, the wet wood pellets (moisture content = 16.4%) are regarded as high permittivity, which is 6.8.

Table VI Comparison of reconstructed images for the segmented moisture distributions.

| Wet area (%) | Targeted distribution | LBP | Tikhonov | Landweber | SIRT | FSBI | Moisture content |
|---|---|---|---|---|---|---|---|
| 10 | | | | | | | 16.4 % |
| 25 | | | | | | | 14.7 % |
| 50 | | | | | | | 12.9 % |
| 75 | | | | | | | 11.2 % |
| 90 | | | | | | | 9.5 % |
| | | | | | | | 7.7 % |

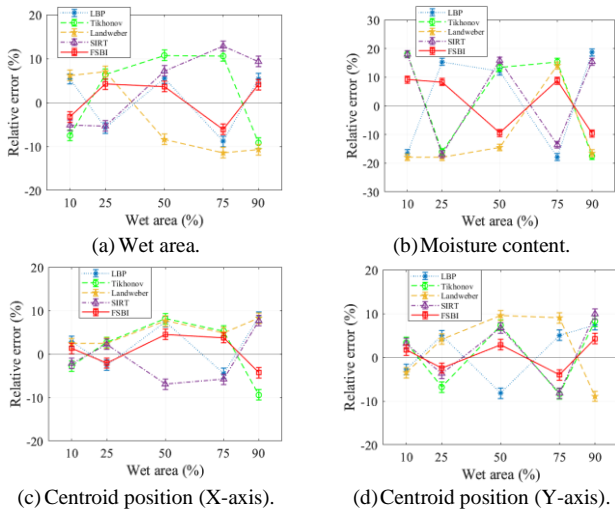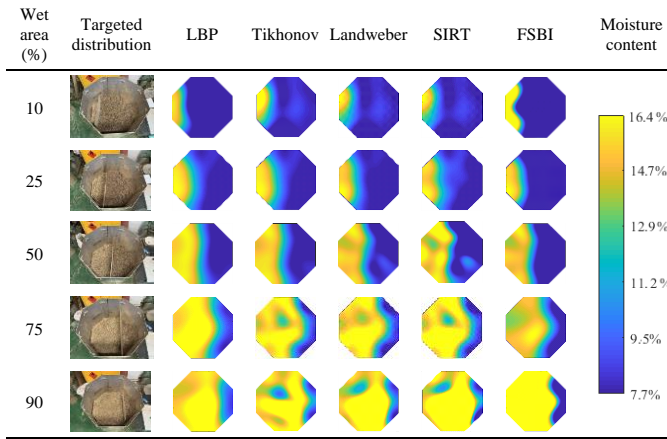Fig. 13. Comparison of relative errors of the wet area, moisture content and centroid position for the segmented moisture distributions.
(a) Wet area.  (b) Moisture content.  (c) Centroid position (X-axis).  (d) Centroid position (Y-axis).

Table VII Comparison of reconstructed images for the oblique moisture distributions.

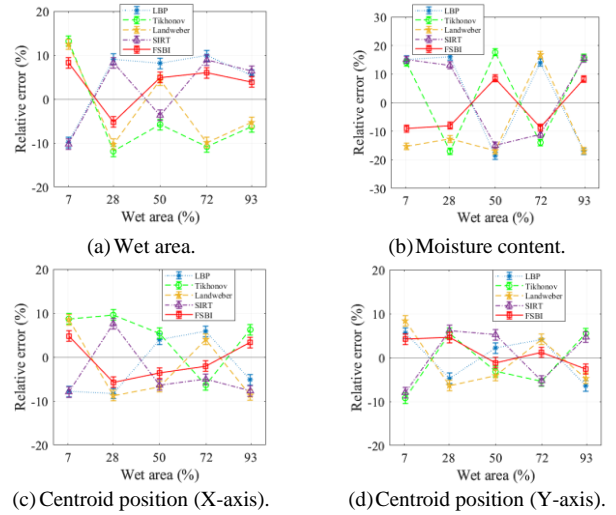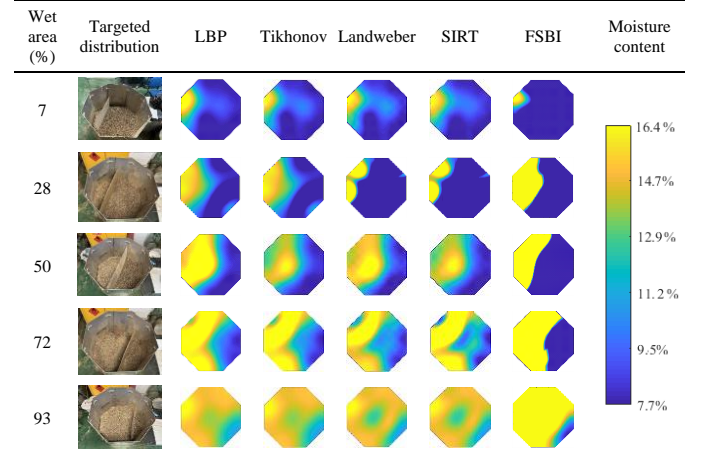| Wet area (%) | Targeted distribution | LBP | Tikhonov | Landweber | SIRT | FSBI | Moisture content |
|---|---|---|---|---|---|---|---|
| 7 | | | | | | | 16.4 % |
| 28 | | | | | | | 14.7 % |
| 50 | | | | | | | 12.9 % |
| 72 | | | | | | | 11.2 % |
| 93 | | | | | | | 9.5 % |
| | | | | | | | 7.7 % |

Fig. 14. Comparison of relative errors of the wet area, moisture content and centroid position for the oblique moisture distributions.
(a) Wet area.  (b) Moisture content.  (c) Centroid position (X-axis).  (d) Centroid position (Y-axis).

### 1) Circular distribution

In the experiments, the cylinders with different diameters were filled with the wet wood pellets. The circular areas are 4%, 9%, 25% and 81% of the silo cross-section, respectively. Through ten repeated experiments, the reconstructed images are shown in Table V. In the reconstructed images, the yellow color represents the wet wood pellets, and the blue color represents the dry wood pellets. Fig. 12 depicts the relative errors of the wet area, centroid position and moisture content.

As illustrated in Table V, it is evident that the reconstructed images from the FSBI algorithm are more similar to the targeted distributions and have fewer artifacts. In Fig. 12, the relative errors of the wet area, centroid position and moisture content from the FSBI algorithm are smaller than the other four algorithms. The relative errors of the wet area, centroid position and moisture content from the FSBI algorithm are within ±8%, ±5% and ±10%, respectively. The experimental results indicate that the ECT is able to measure the circular moisture distribution in a biomass silo with the wet area ranging from 4% to 81%.

### 2) Parallel segmented distribution

Parallel segmented moisture distribution indicates that the moist region starts from one side of the octagon and gradually increases in a parallel direction along the side of the octagon. In the experiments, five segmented moisture distributions are measured and the wet areas are 10%, 25%, 50%, 75% and 90% of the octagonal silo cross-section, respectively. Through ten repeated experiments, the reconstructed images are shown in Table VI. Fig. 13 depicts the relative errors of the wet area, centroid position and moisture content.

It can be seen from Table VI that the reconstructed images using the FSBI algorithm agree well with the targeted distributions, which have fewer artifacts. In summary, the relative error of the wet area from the FSBI algorithm is within ±8% and the relative error of moisture content is within ±10%. Moreover, the centroid position is within ±5% of its expected location.

### 3) Oblique segmented distribution

Oblique segmented moisture distribution means that the moist region starts from an inner angle of the octagon and gradually increases along a diagonal of the octagon. In the experiments, five oblique moisture distributions are investigated. The wet area of the oblique moisture distribution ranges from 7% to 93% of the silo cross-section. Through ten repeated experiments, Table VII shows the reconstruction results of the oblique distributions. Fig. 14 shows the relative errors of the wet area, centroid position and moisture content.

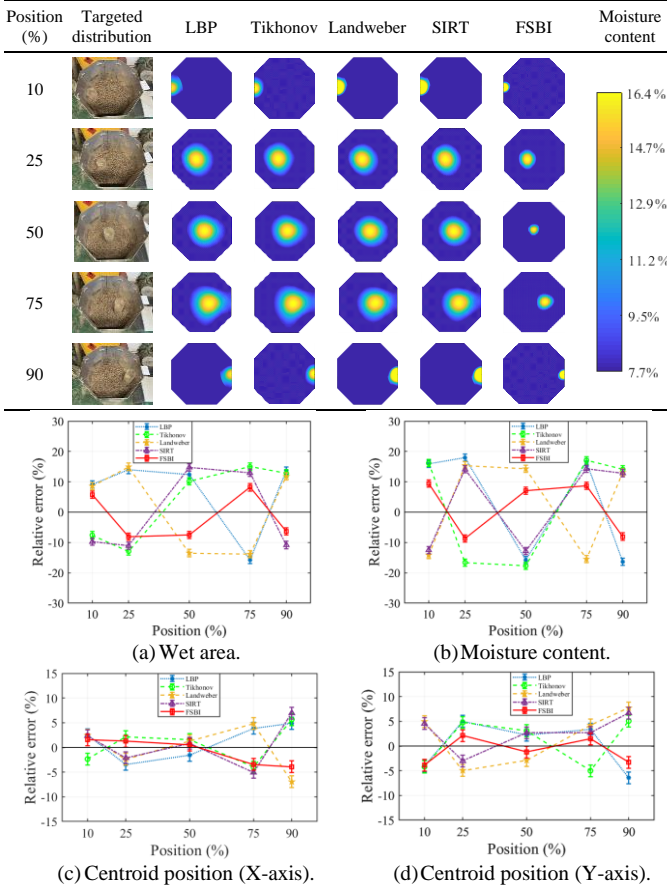Table VIII Reconstructed images when the wet area moves horizontally.

| Position (%) | Targeted distribution | LBP | Tikhonov | Landweber | SIRT | FSBI | Moisture content |
|---|---|---|---|---|---|---|---|
| 10 | | | | | | | 16.4% |
| 25 | | | | | | | 14.7% |
| 50 | | | | | | | 12.9% |
| 75 | | | | | | | 11.2% |
| 90 | | | | | | | 9.5% 7.7% |



(a) Wet area.  (b) Moisture content.
(c) Centroid position (X-axis).  (d) Centroid position (Y-axis).

Fig. 15. Relative errors of the wet area, moisture content and centroid position when the wet area moves horizontally.

Table IX Reconstructed images when the wet area moves obliquely.

| Position (%) | Targeted distribution | LBP | Tikhonov | Landweber | SIRT | FSBI | Moisture content |
|---|---|---|---|---|---|---|---|
| 10 | | | | | | | 16.4% |
| 25 | | | | | | | 14.7% |
| 50 | | | | | | | 12.9% |
| 75 | | | | | | | 11.2% |
| 90 | | | | | | | 9.5% 7.7% |



(a) Wet area.  (b) Moisture content.
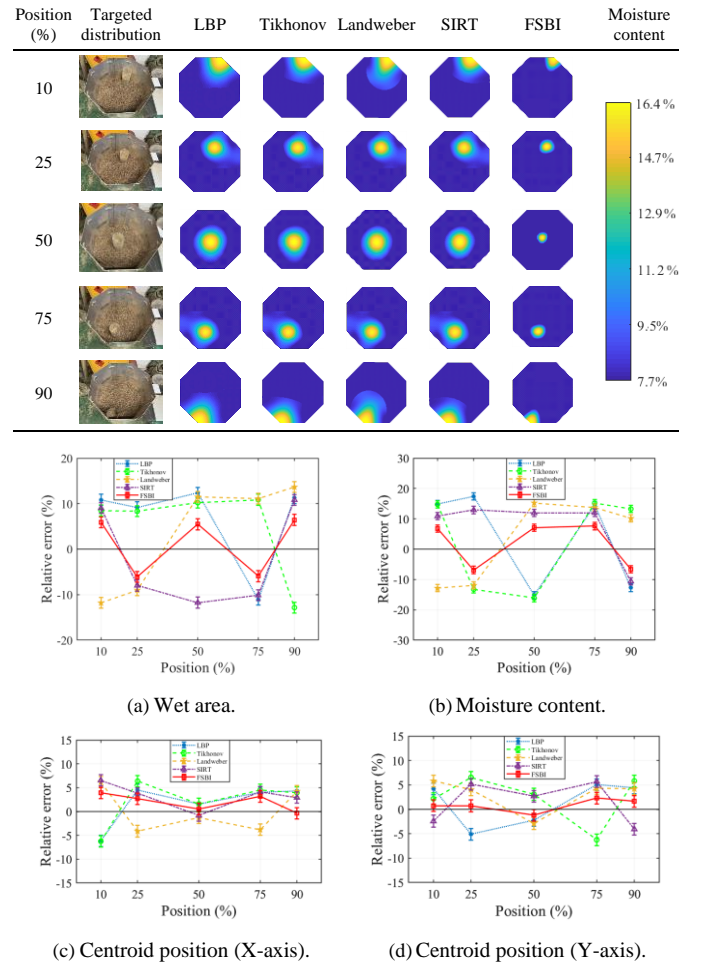(c) Centroid position (X-axis).  (d) Centroid position (Y-axis).

Fig. 16. Relative errors of the wet area, moisture content and centroid position when the wet area moves obliquely.

As illustrated in Table VII, the yellow region in the reconstructed images increases with the wet area. Table VII shows that the reconstruction results obtained with the FSBI algorithm are the best among the five algorithms. Meanwhile, the relative errors of the FSBI algorithm are the smallest. Fig. 14(a) depicts that the relative error of the wet area from the FSBI algorithm is within ±8%. In Fig. 14(c)-(d), the relative errors of the centroid position are within ±5%. Fig. 14(b) indicates that the relative error of the moisture content is within ±10%. In conclusion, the experimental results show that the ECT has the capability to measure the oblique moisture distribution in a biomass silo with the wet area ranging from 7% to 93%.

4) *Parallel movement*

The moisture distribution may occur at different positions in a biomass silo. The cylindrical tube contains the wet wood pellets, which account for 4% of the silo cross-section. In the experiments, the cylindrical tube moved in the horizontal direction. The positions are 10%, 25%, 50%, 75% and 90% of the silo width, respectively. Through ten repeated experiments, Table VIII exhibits the reconstructed images. Fig. 15 shows the relative errors of the wet area, centroid position and moisture content.

When the cylindrical tube moves horizontally, the position and size of the wet area in the biomass silo are observed from the reconstructed images. Table VIII reveals that, compared with all the algorithms mentioned above, the imaging results

reconstructed with the FSBI algorithm are the closest to the targeted distributions. According to the results presented in Fig. 15(a), the relative error of the wet area from the FSBI algorithm is within ±8%. In particular, the relative error of the centroid position is within ±5%. In Fig. 15(b), the relative error of moisture content is within ±10%.

5) *Oblique movement*

In the experiments, the above-mentioned cylindrical tube moved along the diagonal direction in the octagonal silo. The positions are 10%, 25%, 50%, 75%, and 90% of the diagonal length in the octagonal silo. Through ten repeated experiments, Table IX demonstrates the reconstructed images. The relative errors of the wet area, centroid position and moisture content are shown in Fig. 16.

When the cylindrical tube moves in a diagonal direction, the position and size of the tube in the biomass silo are observed in Table IX. When it comes to the results in Fig. 16, the relative errors from the FSBI algorithm are lower than those from the other algorithms. The relative errors of the wet area, centroid position and moisture content from the FSBI algorithm are within ±8%, ±5% and ±10%, respectively.

V.  CONCLUSION

In this paper, ECT has been applied to measure the moisture distribution of wood pellets in a biomass silo. The following conclusions are drawn from the results presented:

1) The experimental results have proven that ECT is capable of obtaining the effective permittivity of wood pellets with different moisture content, ranging from 7.7% to 16.4%.

(2) From the results in Tables I-IX, the FSBI algorithm has given the best reconstruction results amongst the five algorithms, which is more suitable for the reconstruction of the moisture distribution in a biomass silo.

(3) The experimental results have demonstrated that ECT has the capability to measure the moisture distribution within a range of 4% to 93% with a relative error of $\pm 8\%$. Moreover, the relative errors of the centroid position and moisture content from the FSBI algorithm are within $\pm 5\%$ and $\pm 10\%$, respectively.

Although the experimental results reported are the two-dimensional cross-sectional moisture distribution in a biomass silo, ECT has the potential to be deployed for the measurement of three-dimensional moisture distribution, which will be studied in the near future.

## REFERENCES

[1] K. Wiranarongkorn, P. Phajam, K. Im-Orb, D. Saebea and A. Arpornwichanop, "Assessment and analysis of multi-biomass fuels for sustainable electricity generation," *Renew. Energy*, vol. 180, pp. 1405-1408, Dec. 2021.

[2] S. Li, Y. Wu, M. Dao, E. Dragoi and C. Xia, "Spotlighting of the role of catalysis for biomass conversion to green fuels towards a sustainable environment: Latest innovation avenues, insights, challenges, and future perspectives," *Chemosphere*, vol. 318, pp. 137954, Jan. 2023.

[3] H. Alalwan, A. Alminshid, and H. Aljaafari, "Promising evolution of biofuel generations. Subject review," *Renew Energy Focus*, vol. 28, pp. 127-139, Mar. 2019.

[4] F. Shen, L. Zhao, W. L. Du, W. M. Zhong and F. Qian, "Large-scale industrial energy systems optimization under uncertainty: a data-driven robust optimization approach," *Appl. Energy*, vol. 259, Feb. 2020, Art. no. 114199.

[5] H. Mao, F. Wang, F. Mao, Y. Chi and K. Cen, "Measurement of water content and moisture distribution in sludge by 1 H nuclear magnetic resonance spectroscopy," *Drying Technol.*, vol. 34, pp. 267-274, Jan. 2016.

[6] F. Xu, X. Jin, L. Zhang and X. Chen, "Investigation on water status and distribution in broccoli and the effects of drying on water status using NMR and MRI methods," *Food Res. Int.*, vol. 96, pp. 191-197, Jun. 2017.

[7] K. Klingmüller and J. Lelieveld, "Climate model-informed deep learning of global soil moisture distribution," *Geosci. Model Dev.*, vol. 14, pp. 4429-4441, Feb. 2021.

[8] M. Ghijs, B. Vanbillemont, N. Nicolaï, T. D. Beer and I. Nopens, "Two-dimensional moisture content and size measurement of pharmaceutical granules after fluid bed drying using near-infrared chemical imaging," *Int. J. Pharm.*, vol. 595, Feb. 2021, Art. no. 120069.

[9] M. Hallaji, A. Seppänen and M. Pour-Ghaz, "Electrical resistance tomography to monitor unsaturated moisture flow in cementitious materials," *Cem. Concr. Res.*, vol. 69, pp. 10-18, Mar. 2015.

[10] N. Terzija, W. Yin, G. Gerbeth, F. Stefani, K. Timmel, T. Wondrak and A. Peyton, "Electromagnetic inspection of a two-phase flow of gains and argon," *Flow Meas. Instrum.*, vol. 22, pp. 10-16, Mar. 2011.

[11] S. Wang, X. Sun, C. Xu, J. Bao, C. Peng and Z. Tang, "Investigation of a circulating turbulent fluidized bed with a fractal gas distributor by electrostatic-immune electrical capacitance tomography - ScienceDirect," *Powder Technol.*, vol. 361, pp. 562-570, Feb. 2020.

[12] D. Smyl, M. Hallaji, A. Seppaenen and M. Pour-Ghaz, "Quantitative electrical imaging of three-dimensional moisture flow in cement-based materials," *Int. J. Heat Mass Transfer*, vol. 103, pp. 1348-1358, Dec. 2016.

[13] Q. Wang, K. Li, R. Zhang, J. Wang and H. Wang, "Sparse defects detection and 3d imaging base on electromagnetic tomography and total

[14] variation algorithm," *Rev. Sci. Instrum.*, vol. 90, Dec. 2019, Art. no. 124703.

[14] H. Wang and W. Yang, "Application of electrical capacitance tomography in pharmaceutical fluidised beds - A review," *Chem. Eng. Sci.*, vol. 231, Oct. 2021, Art. no. 116236.

[15] A. El-Shafie, M. Osama, M. Hussein, A. El-Gindy and R. Ragab, "Predicting soil moisture distribution, dry matter, water productivity and potato yield under a modified gated pipe irrigation system: saltmed model application using field experimental data," *Agr. Water Manage.*, Vol. 184, pp. 221-233, Apr. 2017.

[16] G Chaplin and T. Pugsley, "Application of electrical capacitance tomography to the fluidized bed drying of pharmaceutical granule," *Chem. Eng. Sci.*, vol. 60, pp. 7022-7033, Dec. 2005.

[17] V. Rimpiläinen, L. Heikkinen and M. Vauhkonen, "Moisture distribution and hydrodynamics of wet granules during fluidized-bed drying characterized with volumetric electrical capacitance tomography," *Chem. Eng. Sci.*, vol. 75, pp. 220-234, Mar. 2005.

[18] H. Wang and W. Yang, "Measurement of fluidised bed dryer by different frequency and different normalisation methods with electrical capacitance tomography," *Powder Technol.*, vol. 199, pp. 60-69, May 2010.

[19] L. Johansson, B. Leckner, L. Gustavsson, D. Cooper, C. Tullin and A. Potter, "Emission characteristics of modern and old-type residential boilers fired with wood logs and wood pellets," *Atmos. Environ.*, vol. 38, pp. 4183-4195, Aug. 2004.

[20] W. Zhang, J. Yan and Y. Yan, "Measurement of the moisture content in woodchips through capacitive sensing and data driven modeling," *Measurement*, vol. 186, Dec. 2021, Art. no. 110205.

[21] R. Dean, A. Rane, M. Baginski, J. Richard, Z. Hartzog and J. David, "A capacitive fringing field sensor design for moisture measurement based on printed circuit board technology," *IEEE Trans. Instrum. Meas.*, vol. 61, pp. 1105-1112, Dec. 2012.

[22] R. Santos, J. Sallese, M. Mattavelli, A. Nunes, C. Dehollain and D. Barrettino, "High precision capacitive moisture sensor for polymers: modeling and experiments," *IEEE Sens. J.*, vol. 20, pp. 3032-3039, Mar. 2020.

[23] G. Guo, Y. Yan, W. Zhang, Y. Hu and G. Fu, "Measurement of moisture distribution in a biomass silo based on electrical capacitance tomography," in *Proc. IEEE Int. Instrum. Meas. Technol. Conf. (I2MTC)*, Kuala Lumpur, Malaysia, May 2023.

[24] B. Perkalskis and J. Freeman, "Examining tensors in the lab: the dielectric permittivity and electrical resistivity of wood," *Am. J. Phys.*, vol. 66, pp. 816-820, Sep. 1988.

[25] J. Nystrom and E. Dahlquist, "Methods for determination of moisture content in woodchips for power plants – a review," *Fuel*, vol. 83, pp. 773–779, May 2004.

[26] K. Alme and S. Mylvaganam, "Electrical capacitance tomography—sensor models, design, simulations, and experimental verification," *IEEE Sens. J.*, vol. 6, pp. 1256-1266, Oct. 2006.

[27] R. Jenkyns, G. Dunn, M. Herzog and J. Faber, "Discussion. calculation of material pressures for the design of soils," *Proc. Inst. Civ. Eng.*, vol. 67, pp. 553-557, Jun. 1979.

[28] W. Zuo, E. Jia, X. Liu, Q. Peng, Y. Deng and H. Zhu, "Orthogonal experimental design and fuzzy grey relational analysis for emitter efficiency of the micro-cylindrical combustor with a step," *Appl. Therm. Eng.*, vol. 103, pp. 945-951, Jun. 2016.

[29] Y. Guan, L. Tai, Z. Cheng, G. Chen, B. Yan and L. Hou, "Biomass molded fuel in china: current status, policies and suggestions," *Sci. Total Environ.*, vol. 724, Jul. 2020, Art. no. 138345.

[30] R. Samuelsson, S. Larsson, M. Thyrel, and T. Lestander, "Moisture content and storage time influence the binding mechanisms in biofuel wood pellets," *Appl. Energy*, vol. 99, pp. 109-115, Nov. 2012.

[31] A. Sihvola and J. Kong, "Effective permittivity of dielectric mixtures," *IEEE Trans. Geosci. Remote Sens.*, vol. 26, pp. 420-429, Jul. 1988.

[32] M. Baidillah1 and M Takei, "Exponential model normalization for electrical capacitance tomography with external electrodes under gap permittivity conditions," *Meas. Sci. Technol.*, vol.28, Jun. 2017, Art. no. 064002.

[33] D, Rainer, "Dimensionally hybrid electric potentials and fields in high-permittivity thin films and interfaces," *Phys. E,* vol.42, pp. 2424-2430, Jul. 2010.

[34] M. Mckeown, S. Trabelsi, S. Nelson and E. Tollner, "Microwave sensing of moisture in flowing biomass pellets," *Biosyst. Eng.*, vol. 155, pp. 152-160, Dec. 2017.

[35] J. Posom, A. Shrestha, W. Saechua and P. Sirisomboon, "Rapid non-destructive evaluation of moisture content and higher heating value of

Leucaena leucocephala pellets using near infrared spectroscopy," *Energy*, vol. 107, pp. 464-472, May 2016.

[36] R. Hickling, W. Wei and D. Hagstrum, "Studies of sound transmission in of stored grain for acoustic of insects," *Appl. Acoust.*, vol. 50, pp. 263-278, Aug. 1997.

[37] S. Ghafghazi, T. Sowlati, S. Sokhansanj, X. Bi and S. Melind, "Particulate matter emissions from combustion of wood in district heating applications," *Renew. Sustain. Energy Rev.*, vol. 15, pp. 3019-3028, Aug. 2011.

[38] M. Sthl, K. Granstrm, J. Berghel and R. Renstrm, "Industrial processes for biomass drying and their effects on the quality properties of wood pellets," *Biomass Bioenerg.*, vol. 27, pp. 621-628, Dec. 2004.

[39] E. Bañuelos-Cabral, J. Gutierrez-Robles and B. Gustavsen, "Rational fitting techniques for the modeling of electric power components and systems using MATLAB environment," *IntechOpen*, Jan. 2017.

[40] Q. Zhao, S. Liu, X. Chai and H. Guo. "A novel computational imaging algorithm based on split Bregman iterative for electrical capacitance tomography," *Meas. Sci. Technol.*, vol. 32, Aug. 2021, Art. no. 125401.

[41] A. Bhandari, I. Kumar and K. Srinivas, "Cuttlefish algorithm-based multilevel 3-d Otsu function for color image segmentation," *IEEE Trans. Instrum. Meas.*, vol. 69, pp. 1871-1880, Jun. 2020.